Impact of Soret Diffusion, Heat Generation/Absorption and Chemical Reactivity on Transient Convection Flow in a Vertical Tube with Ramped Thermal and Concentration Boundaries

Sylvester Bakut Joseph
Department of Mathematics and Statistics,
Nuhu Bamalli Polytechnic, Zaria, Nigeria

Abstract:
This study takes into account the Soret effect, the heat source/sink, and the chemical reaction on a time-dependent natural convection fluid flow through a vertical and infinite tube. A ramped boundary condition for both temperature and concentration is imposed on the wall of the tube. Analytical solutions of the governing equations are obtained with the aid of the Laplace transform and laid out as relations in modified Bessel functions. These solutions are intricate and arduous to invert; thus, a numerical approach, the Riemann sum approximation method, is utilized. A comprehension of the flow pattern is gained by the use of graphs to lay out the temperature, concentration, and velocity, while tables are used to exhibit the skin-friction, Nusselt, and Sherwood numbers. The time-dependent solutions at large time values are compared to the independent closed-form steady-state solutions, which are shown to be in good agreement. The study uncovered that as the heat source and generative chemical reaction increase, the Nusselt and Sherwood numbers, respectively, decrease until flow reversal sets in.

Keywords: Soret effect; Riemann sum; tube; chemical reaction; heat source/sink; ramped

Nomenclature:
C_p Specific heat capacity (J/kgK)
D_C Mass diffusion coefficient (m^2/s)
D_T Thermal diffusion coefficient (m^2/s)
g Acceleration due to gravity (m/s^2)
r Radial coordinate (m)
t Time (s)
u Fluid velocity (m/s)

Greek symbols
α Thermal diffusivity (m^2/s)
β_T Coefficient of thermal expansion $(1/K)$
β_C Mass expansion coefficient (m^3/kg)
ν Kinematic viscosity (m^2/s)
ϕ Fluid concentration (kg/m^3)
θ Fluid temperature (K)
ρ Fluid density (kg/m^3)
τ Skin friction

Introduction:
Free convection flows in confined geometries are significant because of their prevalence in various engineering, geophysical, and environmental systems. These configurations include the vertical tube which is of particular interest because it has application in nuclear reactor cooling channels, geothermal reservoirs, underground thermal storage, chemical reactors, and double-pipe heat exchangers (Jha & Oni, 2019). In applications like these, flows induced by buoyancy often interact with other transport phenomena like internal heating or cooling, chemical reactions, and cross-diffusion effects. Comprehending the combined influence of these processes under transient boundary conditions is crucial for accurately predicting system behavior, optimizing performance, and ensuring safety

https://doi.org/10.5281/zenodo.17251831

margins for both thermal and chemical processes.

The role played by transient convection is critical in startup and shutdown processes, where the momentum, temperature, and concentration fields undergo a dynamic evolution before achieving steady conditions. Ramped wall temperature and surface concentration introduce gradual changes, not sudden jumps, which represent industrial heating, cooling, and mass transfer operations more realistically (Jha et al., 2024; Kumar, 2016). These ramped conditions effectively lessen the occurrence of sharp gradients during the initial phases, resulting in more gradual and controlled transient development and preventing destabilizing overshoots in transport profiles. (Jha & Gambo, 2019, 2020a). Boundary conditions modelled in this manner capture the actual thermal and solutal histories of systems ranging from catalytic reactors to heat exchangers and biomedical devices.

Heat generation or absorption, modeled as volumetric source or sink terms, further complicates natural convection transport. Internal heat sources may arise from exothermic reactions, Joule heating, or radioactive decay, while sinks represent endothermic processes or localized energy removal. The presence of heat generation increases buoyancy forces, steepens thermal gradients, and enhances velocity fields, whereas absorption counteracts buoyancy and reduces flow strength (Dwivedi et al., 2023; Parasuraman & Babu, 2024). The coupling between heat source/sink effects and ramped boundaries is especially important in tubular systems, where thermal management directly affects efficiency and safety.

Chemical reaction mechanisms within the fluid medium add another layer of complexity. Generative reactions increase solute concentration and buoyancy, amplifying convective intensity, while destructive reactions deplete solute and attenuate flow (Harikrushna et al., 2023). In energy systems, polymerization reactors, and biochemical processes, chemical kinetics strongly influence solutal boundary layers, altering both momentum and heat transfer rates (Pal & Mondal, 2011). When combined with internal heat sources and ramped boundaries, chemical reactions create nonlinear feedback loops that govern the temporal evolution of the system.

Cross-diffusion phenomena, especially thermal diffusion, otherwise known as the Soret effect, are critical factors in coupled heat and mass transfer. Imposed temperature gradients give rise to the Soret effect, which drives species movement to seeding solutal stratification that can either enhance or counteract thermal buoyancy. This coupling significantly changes the relative contributions of thermal and solutal buoyancy forces particularly in reactive or systems of multiple components (Jha & Gambo, 2020b; Shah et al., 2023). For instance, in a heated vertical tube filled with a reactive fluid, the redistribution of solutes caused by thermal diffusion can enhance generative reactions or inhibit destructive ones, leading to complex dynamics of velocity and concentration. The effect becomes more significant when transient ramped conditions, where time-dependent gradients continuously change the diffusion process, are employed (Umavathi et al., 2022).

Recent analytical and computational studies have addressed these interacting effects in various geometries. Jha and Oni (2016, 2019) examined natural convection in vertical tubes and annuli under time-periodic and ramped heating, highlighting the moderating influence of ramped conditions. Gambo and Jha (2020) extended this framework by including Soret and Dufour effects in transient vertical channels with ramped temperature and concentration, providing evidence of strong cross-diffusion impacts. Dwivedi et al. (2023) and Harikrushna et al. (2023) investigated chemically reactive fluids with internal heat sources, showing that reactions coupled with heating mechanisms can dramatically alter velocity and solutal distributions. Similarly, Shah et al. (2023) and Tayebi et al. (2023) analyzed double-diffusive convection with Soret/Dufour effects, confirming their pivotal role in multicomponent flows.

Despite these advances, comprehensive analyses that simultaneously account for

https://doi.org/10.5281/zenodo.17251831

ramped boundary heating and concentration, internal heat source/sink, chemical reactivity, and Soret diffusion in vertical tubular geometries remain limited. Most previous studies have focused on specific combinations of these mechanisms—such as ramped boundary conditions with heat sources (Kumar & Vatsa, 2016), chemical reactions in porous channels (Pal & Mondal, 2011), or Soret/Dufour effect in ducts and enclosures (Umavathi et al., 2022; Tayebi et al., 2023).. The combined problem represents realistic operating conditions in systems like geothermal wells, catalytic reactors, and nuclear waste repositories, where thermal ramping, chemical reaction, and cross-diffusion all act simultaneously.

This analysis, therefore, addresses a significant research gap by investigating the transient convection flow of a chemically reactive fluid in a vertical tube subjected to ramped wall temperature and ramped surface concentration, incorporating the joint effects of thermal diffusion and heat generation or absorption. By employing a semi-analytical framework, the study captures the unsteady development of velocity, temperature, and concentration fields, thereby extending existing literature on transient buoyancy-driven flows. The results are expected to provide deeper insight into the interplay between energy sources, chemical kinetics, and cross-diffusion, and to contribute to the design and optimization of heat and mass transfer processes in tubular geometries.

Mathematical Analysis:

A viscous, incompressible heat source/sink fluid's transient natural convection flow through a pipe is considered. The radius of the pipe is γ_1, and the fluid flows vertically along the z'-axis of the pipe with the radial direction (γ'-axis) perpendicular to it (Figure 1). At the start ($\zeta' = 0$), the fluid and wall of the pipe have identical temperatures θ_0 and concentrationsϕ_0. Later ($\zeta' > 0$), the wall of the pipe assumes ramped functions $\theta_0 + (\theta_w - \theta_0)\frac{\zeta'\nu}{{\gamma_1}^2\zeta_1}$ and $\phi_0 + (\phi_w - \phi_0)\frac{\zeta'\nu}{{\gamma_1}^2\zeta_1}$ respectively when $\zeta' \le {\gamma_1}^2\zeta_1/\nu$ and takes constant values of θ_w and ϕ_w respectively when $\zeta' > {\gamma_1}^2\zeta_1/\nu$ where ζ_1 is a reference time for the ramped boundary conditions. The flow depends on γ' and ζ' due to the consideration of fully developed characteristics. The Soret effect, a chemical reaction, and a heat source/sink are considered in the fluid. Imposing the Boussinesq approximation where all other forces are considered constant except the force of gravity,

The model is expressed as follows:

$$\frac{\partial u'}{\partial \zeta'} = \nu\frac{1}{\gamma'}\frac{\partial}{\partial \gamma'}\left(\gamma'\frac{\partial \omega'}{\partial \gamma'}\right) + g\beta_T(\theta' - \theta_0) + g\beta_C(\phi' - \phi_0), \tag{1}$$

$$\frac{\partial \theta'}{\partial \zeta'} = \alpha\frac{1}{\gamma'}\frac{\partial}{\partial \gamma'}\left(\gamma'\frac{\partial \theta'}{\partial \gamma'}\right) - \frac{H'}{\rho C_p}(\theta' - \theta_0), \tag{2}$$

$$\frac{\partial \phi'}{\partial \zeta'} = D_C\frac{1}{\gamma'}\frac{\partial}{\partial \gamma'}\left(\gamma'\frac{\partial \phi'}{\partial \gamma'}\right) + D_T\frac{1}{\gamma'}\frac{\partial}{\partial \gamma'}\left(\gamma'\frac{\partial \theta'}{\partial \gamma'}\right) - K'(\phi' - \phi_0). \tag{3}$$

The conditions suitable for the above model are:

$$\left.\begin{array}{ll} 0 \le \gamma' \le \gamma_1,\ u' = 0, \theta' = \theta_0, \phi' = \phi_0 & \text{for} \zeta' \le 0. \\ \gamma' = 0, \frac{\partial u'}{\partial \gamma'} = \frac{\partial \theta'}{\partial \gamma'} = \frac{\partial \phi'}{\partial \gamma'} = 0 & \text{for} \zeta' > 0. \\ \gamma' = \gamma_1, u' = 0 \left\{\begin{array}{l} \theta' = \theta_0 + (\theta_w - \theta_0)\frac{\zeta'\nu}{{\gamma_1}^2\zeta_1} \\ \phi' = \phi_0 + (\phi_w - \phi_0)\frac{\zeta'\nu}{{\gamma_1}^2\zeta_1} \end{array}\right\} & \text{for } 0 < \zeta' < \frac{{\gamma_1}^2\zeta_1}{\nu}, \\ \theta' = \theta_w, \phi' = \phi_w & \text{for} \zeta' \ge \frac{{\gamma_1}^2\zeta_1}{\nu}. \end{array}\right\} \tag{4}$$

Express the following parameters:

$$r = \gamma'/\gamma_1, t = \frac{\zeta'\nu}{{\gamma_1}^2}, \theta = \frac{\theta' - \theta_0}{\theta_w - \theta_0}, \phi = \frac{\phi' - \phi_0}{\phi_w - \phi_0}, \text{and } u = \frac{\nu u'}{g{\gamma_1}^2\beta_T(\theta_w - \theta_0)} \tag{5}$$

https://doi.org/10.5281/zenodo.17251831

Equations (1)-(3) will then be transformed by the use of (5) to obtain the following non-dimensional equations:

$$\frac{\partial u}{\partial t} = \frac{1}{r}\frac{\partial}{\partial r}\left(r\frac{\partial u}{\partial r}\right) + \theta + N\phi, \tag{6}$$

$$\frac{\partial \theta}{\partial t} = \frac{1}{Pr}\frac{1}{r}\frac{\partial}{\partial r}\left(r\frac{\partial \theta}{\partial r}\right) - H\theta, \tag{7}$$

$$\frac{\partial \phi}{\partial t} = \frac{1}{Sc}\frac{1}{r}\frac{\partial}{\partial r}\left(r\frac{\partial \phi}{\partial r}\right) + St\frac{1}{r}\frac{\partial}{\partial r}\left(r\frac{\partial \theta}{\partial r}\right) - K\phi, \tag{8}$$

Where the Soret, Prandtl, and Schmidt numbers are defined as $St = D_T(\theta_w - \theta_0)/D_C(\phi_w - \phi_0)$, $Pr = \upsilon/\alpha$ and $Sc = \upsilon/D_C$, respectively. Also, the heat source/sink and chemical reaction parameters in the dimensionless form are given as $H = H'\gamma_1{}^2/\nu\rho C_p$ and $K = K'\gamma_1{}^2/\nu$, finally, $N = \beta_C(\phi_w - \phi_0)/\beta_T(\theta_w - \theta_0)$ is the buoyancy ratio. Conditions (4) are also rendered dimensionless by (5) to become:

$$\left.\begin{array}{l} 0 \le r \le 1,\ u = 0, \theta = 0, \phi = 0 \ \text{ for } \ t \le 0. \\ r = 0,\ \frac{\partial u}{\partial r} = \frac{\partial \theta}{\partial r} = \frac{\partial \phi}{\partial r} = 0 \quad \text{for} \quad t > 0. \\ r = 1, u = 0 \begin{cases} \theta = \frac{t}{\zeta_1} \\ \phi = \frac{t}{\zeta_1} \end{cases} \text{for } 0 < t \le \zeta_1, \\ \theta = 1, \phi = 1 \quad \text{for} \quad t \ge \zeta_1. \end{array}\right\} \tag{9}$$

The Heaviside step function unifies the temperature and concentration at $r = 1$ as

$$\theta = \phi = \frac{1}{\zeta_1}[tH(t) - (t - \zeta_1)H(t - \zeta_1)] \tag{10}$$

Let $\bar{u}(r,s) = \int_0^\infty u(r,t)\exp(-st)dt$, $\bar{\theta}(r,s) = \int_0^\infty \theta(r,t)\exp(-st)dt$, and $\bar{\phi}(r,s) = \int_0^\infty \phi(r,t)\exp(-st)\,dt$ be the Laplace transforms of the velocity, temperature, and concentration respectively. Also, let $\epsilon_1 = \Pr(s + H)$, $\epsilon_2 = \mathrm{Sc}(s + K)$, then equations (6)–(8) are transformed to:

$$\frac{1}{r}\frac{d}{dr}\left(r\frac{d\bar{u}}{dr}\right) - s\bar{u} = -\bar{\theta} - N\bar{\phi} \tag{11}$$

$$\frac{1}{r}\frac{d}{dr}\left(r\frac{d\bar{\theta}}{dr}\right) - \epsilon_1\bar{\theta} = 0 \tag{12}$$

$$\frac{1}{r}\frac{d}{dr}\left(r\frac{d\bar{\phi}}{dr}\right) + St\frac{1}{r}\frac{d}{dr}\left(r\frac{d\bar{\theta}}{dr}\right) - \epsilon_2\bar{\phi} = 0 \tag{13}$$

Using equation (12) in (13), we obtain:

$$\frac{1}{r}\frac{d}{dr}\left(r\frac{d\bar{\phi}}{dr}\right) + St\epsilon_1\bar{\theta} - \epsilon_2\bar{\phi} = 0 \tag{14}$$

Also, the boundary conditions (9) reduces to:

$$\left.\begin{array}{l} \frac{d\bar{u}}{dr} = \frac{d\bar{\theta}}{dr} = \frac{d\bar{\phi}}{dr} = 0 \quad \text{at } r = 0 \\ \bar{u} = 0, \bar{\theta} = \bar{\phi} = \frac{1-\exp(-s\zeta_1)}{\zeta_1 s^2} \text{at } r = 1 \end{array}\right\} \tag{15}$$

Solutions:

The solution of equation (12) is first obtained analytically. It is then used to get the solution of equation (14), and finally, equation (11) is solved for the velocity using the solutions obtained from equations (12) and (14). These solutions are given:

$$\bar{\theta}(r,s) = \epsilon_3\frac{I_0(r\sqrt{\epsilon_1})}{I_0(\sqrt{\epsilon_1})} \tag{16}$$

$$\bar{\phi}(r,s) = \epsilon_3\left[\left(1 + \frac{\epsilon_1 St}{\epsilon_1 - \epsilon_2}\right)\frac{I_0(r\sqrt{\epsilon_2})}{I_0(\sqrt{\epsilon_2})} - \left(\frac{\epsilon_1 St}{\epsilon_1 - \epsilon_2}\right)\frac{I_0(r\sqrt{\epsilon_1})}{I_0(\sqrt{\epsilon_1})}\right] \tag{17}$$

$$\bar{u}(r,s) = \epsilon_3\left[\frac{1}{\epsilon_1 - s}\left(1 - \frac{N\epsilon_1 St}{\epsilon_1 - \epsilon_2}\right)\left(\frac{I_0(r\sqrt{s})}{I_0(\sqrt{s})} - \frac{I_0(r\sqrt{\epsilon_1})}{I_0(\sqrt{\epsilon_1})}\right) + \frac{N}{\epsilon_2 - s}\left(1 + \frac{\epsilon_1 St}{\epsilon_1 - \epsilon_2}\right)\left(\frac{I_0(r\sqrt{s})}{I_0(\sqrt{s})} - \frac{I_0(r\sqrt{\epsilon_2})}{I_0(\sqrt{\epsilon_2})}\right)\right] \tag{18}$$

where $\epsilon_3 = \frac{1-\exp(-s\zeta_1)}{\zeta_1 s^2}$

https://doi.org/10.5281/zenodo.17251831

Isothermal temperature and concentration wall:

When the reference time is very small i.e. $\varsigma_1 \to 0$, the ramped boundary conditions behave like isothermal boundary conditions. Under this circumstance, the expressions of the ramped temperature, concentration, and velocity presented in equations (16)-(18) will be reduced to the following isothermal form.

$$\bar{\theta}(r,s) = \frac{I_0(r\sqrt{\epsilon_1})}{sI_0(\sqrt{\epsilon_1})}$$

$$\bar{\phi}(r,s) = \frac{1}{s}\left[\left(1+\frac{\epsilon_1 St}{\epsilon_1-\epsilon_2}\right)\frac{I_0(r\sqrt{\epsilon_2})}{I_0(\sqrt{\epsilon_2})} - \left(\frac{\epsilon_1 St}{\epsilon_1-\epsilon_2}\right)\frac{I_0(r\sqrt{\epsilon_1})}{I_0(\sqrt{\epsilon_1})}\right] \quad (20)$$

$$\bar{u}(r,s) = \frac{1}{s}\left[\frac{1}{\epsilon_1-s}\left(1-\frac{N\epsilon_1 St}{\epsilon_1-\epsilon_2}\right)\left(\frac{I_0(r\sqrt{s})}{I_0(\sqrt{s})} - \frac{I_0(r\sqrt{\epsilon_1})}{I_0(\sqrt{\epsilon_1})}\right) + \frac{N}{\epsilon_2-s}\left(1+\frac{\epsilon_1 St}{\epsilon_1-\epsilon_2}\right)\left(\frac{I_0(r\sqrt{s})}{I_0(\sqrt{s})} - \frac{I_0(r\sqrt{\epsilon_2})}{I_0(\sqrt{\epsilon_2})}\right)\right] \quad (21)$$

Rate of Heat Transfer($\square\square$), Rate of Mass Transfer($\square\square$), and Skin Friction($\square$):

The fluid's behavior on the pipe's wall is vital to scientists and engineers. Thus, the solutions of the rate of heat transfer represented by the Nusselt number, the rate of mass transfer represented by the Sherwood number, and the shear stress or skin friction are obtained by the derivatives of the temperature ($\overline{\square}$), concentration ($\overline{\square}$), and velocity ($\overline{\square}$) of equations (16)-(18) respectively at $\square = 1$.

Equation (16) gives $\square\square$ as:

$$\overline{\square\square} = \frac{\square\overline{\square}}{\square\square} = \square_3\frac{\sqrt{\square_1}\square_1(\sqrt{\square_1})}{\square_0(\sqrt{\square_1})} \quad (22)$$

Equation (17) displays $\square h$ as:

$$\overline{\square h} = \frac{\square\overline{\square}}{\square\square} = \square_3\left[\left(1+\frac{\square_1\square\square}{\square_1-\square_2}\right)\frac{\sqrt{\square_2}\square_1(\sqrt{\square_2})}{\square_0(\sqrt{\square_2})} - \left(\frac{\square_1\square\square}{\square_1-\square_2}\right)\frac{\sqrt{\square_1}\square_1(\sqrt{\square_1})}{\square_0(\sqrt{\square_1})}\right] \quad (23)$$

Equation (18) gives $\square$ as: $\overline{\square} = -\frac{\square\overline{\square}}{\square\square} =$

$$\square_3\left[\frac{1}{\square_1-\square}\left(1-\frac{\square\square_1\square\square}{\square_1-\square_2}\right)\left(\frac{\sqrt{\square}\square_1(\sqrt{\square})}{\square_0(\sqrt{\square})} - \frac{\sqrt{\square_1}\square_1(\sqrt{\square_1})}{\square_0(\sqrt{\square_1})}\right) + \frac{\square}{\square_2-\square}\left(1+\frac{\square_1\square\square}{\square_1-\square_2}\right)\left(\frac{\sqrt{\square}\square_1(\sqrt{\square})}{\square_0(\sqrt{\square})} - \frac{\sqrt{\square_2}\square_1(\sqrt{\square_2})}{\square_0(\sqrt{\square_2})}\right)\right] \quad (24)$$

The Laplace Transform inversion:

The inversion of equations (16) - (24) is done by the Riemann-sum approximation method (Khadrawi & Al-Nimr, 2007) as:

$$\Pi(\square,\square) \cong \frac{\exp(\square\square)}{\square}\left[\frac{1}{2}\overline{\Pi}(\square,\square) + \square\square\sum_{\square=1}^{\square}\overline{\Pi}\left(\square,\square+\frac{\square\square\square}{\square}\right)(-1)^{\square}\right] \quad (25)$$

In equation (25), $\Pi(\square,\square)$ represents functions in the Laplace domain, whereas $\Pi(\square,\square)$ represents any inverted function to the time domain. Further, $\square\square$ denotes the "real part of" and $\square = \sqrt{-1}$ symbolizes the imaginary number. The Riemann-sum approximation employs a number of terms which in this study is denoted by $\square$. Inverting the Laplace transforms requires a real part of the Bromwich contour which is given by $\square$ and must be selected to enclose all the branch points. There is a single summation for the numerical process of the Riemann-sum approximation which accuracy is established by the value of $\square$ and the truncation error dictated by $\square$. From numerous numerical experiments, the relation $\square\square \cong 4.7$ which is independent of the value of $\square$ gives the most satisfactory results for faster convergence (Tzou, 1997).

Steady-state:

When $\square/\square\square \to 0$, i.e. as $\square \to \infty$ or $\square \to 0$, the fluid flow approaches steady-state. Under this circumstance, the expression of the velocity presented in equation (18) will be reduced to the following form.

$$\overline{\square}(\square) = \frac{\square}{\square\square\square}\left[\left(1+\frac{\square\square\square\square\square}{\square\square\square-\square\square\square}\right)\left(1-\frac{\square_0(\square\sqrt{\square\square\square\square})}{\square_0(\sqrt{\square\square\square})}\right) + \frac{1}{\square\square\square}\left(1-\frac{\square\square\square\square\square\square}{\square\square\square-\square\square\square}\right)\left(1-\frac{\square_0(\square\sqrt{\square\square\square\square})}{\square_0(\sqrt{\square\square\square})}\right)\right] \quad (26)$$

Validation of the solution method

A numerical solution method in Matlab, PDEPE, and the steady state of equation (26) were used to validate our current work. The numerical values of the PDEPE and the steady state are presented in Table 2.

Results and Discussion:

https://doi.org/10.5281/zenodo.17251831

Figures 2–11 demonstrate how thermal, concentration, and velocity distributions change in response to time-dependent variations of various physical parameters.

In Figure 2, the temperature of the wall jumps instantly during isothermal heating, which drives more heat toward the center of the tube, causing the temperature to rise over time until it reaches a steady state. In contrast, ramped heating results in a gradual temperature increase, leading to a smoother and more controlled transition to the steady state. Although both eventually converge to the same peak temperature, the slower rise in ramped heating shows that it is lower than the isothermal heating at any time. Additionally, isothermal heating produces sharper temperature gradients at the wall compared to ramped heating up until the steady state is achieved.

Figure 3 illustrates that as the heat source ($\square < 0$) increases, the fluid temperature rises and the profiles broaden. In contrast, when the heat sink ($\square > 0$) increases, there is an absorption of energy, leading to a decrease in temperature and sharper gradients. This observation aligns with earlier studies (Chamkha et al., 2001; Molla et al., 2005). Additionally, the Prandtl number significantly influences the profiles. For higher values of the Prandtl number (e.g., $\square\square = 7.0$), heat remains concentrated near the wall, resulting in steep gradients. In comparison, lower Prandtl numbers (e.g., $\square\square = 0.71$) allow for deeper penetration and flatter profiles due to increased thermal diffusivity.

Figure 4 shows that as time progresses, diffusion increases, leading to thicker concentration profiles. The figure also highlights an instantaneous jump in wall concentration for isothermal boundaries, resulting in steep initial gradients and rapid penetration toward the center. In contrast, the concentration for ramped boundaries rises gradually, featuring low initial gradients and slower penetration. As time continues, the difference between the two cases diminishes, with both approaches ultimately reaching the same steady-state distribution. This indicates that ramped concentration smooths the transient response, while isothermal causes a more dramatic increase.

Figure 5 illustrates how concentration profiles vary with the influence of a heat source or sink and different Prandtl numbers. It shows that for a Prandtl number ($\square\square$) of 0.71, an increase in heat source ($\square < 0$) lowers the concentration, while the presence of a sink ($\square > 0$) increases the concentration throughout the flow domain. This occurs because a heat source raises thermal energy and buoyancy, which dilutes the solute, whereas a sink reduces thermal energy and buoyancy, resulting in a higher concentration of the solute.

This behavior is particularly evident near the wall when $\square\square = 7.0$. However, as we move further away from the wall of the tube, the effects of the source and sink begin to change. This shift is attributed to the low thermal diffusivity of fluids with high Prandtl numbers. Additionally, the Prandtl number influences the concentration profiles; as $\square\square$ increases, thermal diffusivity decreases, leading to higher solute concentrations.

Figure 6 shows how the Schmidt number ($\square\square$) affects concentration profiles. At low Schmidt numbers, diffusivity is high, which causes the solute to spread uniformly and results in flatter concentration profiles. As the Schmidt number increases, mass diffusivity decreases, leading to a more confined penetration of the solute within a thinner layer close to the wall. This change steepens the concentration gradients, reduces the thickness of the concentration boundary layers, and slows down the diffusion process towards the center.

Figure 7 illustrates how a generative reaction ($\square < 0$) leads to an increase in species production, which raises concentrations and thickens the solutal layer. In contrast, a destructive reaction ($\square > 0$) consumes species, resulting in lower concentrations and sharper near-wall gradients. Additionally, the Soret number enhances thermo-solutal coupling and profile thickening, further elevating the concentration profiles.

Figure 8 illustrates that velocity increases over time as buoyancy develops. Initially, this velocity is small and occurs near the wall;

https://doi.org/10.5281/zenodo.17251831

however, it subsequently strengthens across the radius and ultimately flattens as the gradients diminish. Under isothermal boundary conditions, the initial full wall driving potential results in stronger early acceleration and higher velocities, whereas ramped heating yields a more gradual increase in growth and smoother transients. At later times, both cases converge to the same velocity distribution, which is the steady state.

Figure 9 demonstrates that a heat source ($\square < 0$) enhances buoyancy, resulting in increased velocity magnitudes. In contrast, a heat sink ($\square > 0$) absorbs energy, thereby weakening buoyancy and diminishing the strength of the flow. Furthermore, the Prandtl number is a critical factor, as an increase in the Prandtl number confines heating near the wall due to reduced thermal diffusivity, ultimately leading to diminished velocity profiles.

Figure 10 illustrates that an increase in the Schmidt number ($\square\square$), which corresponds to a decrease in mass diffusivity, hinders the fluid's acceleration and diminishes the velocity profiles, resulting in reduced convection speeds to the center of the tube.

Figure 11 illustrates that a generative reaction ($\square < 0$) results in an increase in species concentration, enhances solutal buoyancy, and consequently elevates velocities throughout the radius. Conversely, a destructive reaction ($\square > 0$) leads to the consumption of species, diminishes buoyancy, and subsequently reduces velocities. Furthermore, the Soret number further influences the velocity, as a more pronounced thermo-diffusion facilitates additional solute movement along temperature gradients, thereby enhancing interior momentum and flattening the velocity profile. In contrast, a smaller Soret number exhibits weaker coupling and results in less pronounced speeds.

Table 1 demonstrates that the rates of heat transfer ($\square\square$) and mass transfer ($\square h$) metrics exhibit consistent physical behavior as time progresses. The initially high wall gradients generated at start-up reach a peak and subsequently decay towards their equilibrium values over time. The skin friction is observed to increase monotonically as time advances. The presence of a heat source contributes to the warming of the bulk fluid and diminishes the wall temperature gradient, which tends to lower $\square\square$ and elevate $\square h$. Conversely, a heat sink intensifies that gradient, resulting in an increase in $\square\square$ while decreasing $\square h$; the same buoyancy modulation affects the skin friction depending on the orientation of buoyancy, with $\square < 0$ leading to an increase and $\square > 0$ leading to a decrease.

Increasing the Prandtl number, indicative of decreased thermal diffusivity, results in a thinner thermal boundary layer, thereby increasing $\square\square$ while reducing $\square h$ and the near-wall shear. In the context of reactions, generative reactions lead to elevated interior concentrations, which reduce the wall concentration gradient and, consequently, diminish $\square h$. In contrast, destructive reactions accentuate that gradient, thereby increasing $\square h$; the associated buoyancy changes influence skin friction accordingly. An increase in the Schmidt number, reflecting decreased mass diffusivity, results in a thinner concentration boundary layer that promotes a higher $\square h$ and lower shear stress. Furthermore, a higher Soret number enhances thermo-diffusion coupling, typically resulting in increased $\square h$ and a modest rise in shear through enhanced solutal buoyancy. These observed trends align with the summarized values and comparisons presented in Table 1.

Table 2 presents a validation of the Riemann Sum Approximation (RSA) method employed as compared to a PDEPE numerical scheme and the exact solution (ES). The findings indicate that the RSA values exhibit a close correspondence with both PDEPE and ES across various positions and times, with only minimal discrepancies occurring in the third or fourth decimal place. For instance, at $\square = 0.2$ the velocity measurements from RSA and PDEPE differ by less than 10^{-4}, and RSA aligns nearly identically with ES at steady state. This high degree of concordance illustrates that RSA is both accurate and reliable, effectively capturing flow behavior without significant numerical error.

https://doi.org/10.5281/zenodo.17251831

Conclusion:

The study highlights how transient heat and mass transfer in a vertical tube, under varying boundary conditions, is significantly affected by time, thermal-solutal conditions, and different transport parameters. As time progresses, the fields of temperature, concentration, and velocity gradually evolve and approach a steady state. Utilizing ramped heating and concentration produces smoother transitions compared to the sharper gradients typically seen with isothermal conditions. The introduction of a heat source raises both temperature and velocity while simultaneously decreasing concentration. This effect results in a lower Nusselt number, but an increase in both the Sherwood number and skin friction. Conversely, a heat sink cools the fluid, increases solute concentration, enhances the Nusselt number, and reduces flow intensity.

Additionally, higher Prandtl numbers tend to localize heat near the wall, which steepens the gradients and reduces velocity, while lower Prandtl numbers encourage a more uniform distribution of heat. An increase in the Schmidt number restricts solute diffusion, creating steeper concentration gradients that raise Sherwood numbers and decrease velocities. Generative chemical reactions elevate solute levels and buoyancy, subsequently increasing velocity but decreasing mass transfer efficiency. In contrast, destructive reactions consume solute, reduce buoyancy, diminish velocity, and intensify the concentration gradient at the wall. Finally, the Soret effect enhances the coupling between thermo-diffusion, thickening solutal layers, increasing velocity, and modestly improving both heat and mass transfer at the wall. Overall, these findings illustrate the complex interaction of energy sources, cross-diffusion, and chemical kinetics in influencing transient convective transport within tubular systems.

References:

Chamkha, A. J., Takhar, H. S., & Soundalgekar, V. M. (2001). Radiation effects on free convection flow past a semi-infinite vertical plate with mass transfer. Chemical Engineering Journal, 84(3), 335–342. https://doi.org/10.1016/S1385-8947(00)00378-8

Dwivedi, N., Singh, A. K., & Sacheti, N. C. (2023). Influence of temperature-dependent heat source/sink on transient MHD free convective flow in an infinite rigid impermeable vertical cylinder with chemical reaction. Propulsion and Power Research, 12(4), 568–583. https://doi.org/10.1016/j.jppr.2023.11.003

Harikrushna, M., Singh, V. K., & Pandey, A. K. (2023). Chemical reaction effects on magnetohydrodynamic convective flow past a vertical absorbent plate with ramped wall temperature and concentration. Heat Transfer—Asian Research, 52(8), 7498–7523. https://doi.org/10.1002/htj.22856

Jha, B. K., & Gambo, Y. Y. (2019). Dufour effect with ramped wall temperature and specie concentration on natural convection flow through a channel. Physics, 1(1), 111–130. https://doi.org/10.3390/physics1010012

Jha, B. K., & Gambo, Y. Y. (2020b). Soret and Dufour effects on transient free convection heat and mass transfer flow in a vertical channel with ramped wall temperature and specie concentration: An analytical approach. Arab Journal of Basic and Applied Sciences, 27(1), 344–356. https://doi.org/10.1080/25765299.2020.1824392

Jha, B. K., & Gambo, Y. Y. (2020b). Transient natural convection heat and mass transfer flow in a vertical channel in the presence of Soret and Dufour effects: An analytical approach. International Journal of Modern Physics C, 31(15), 2050032. https://doi.org/10.1142/S0129183120500321

Jha, B. K., & Oni, M. O. (2016). Natural convection flow in a vertical tube inspired by time-periodic heating at the surface of the tube. Alexandria Engineering Journal, 55(3), 2827–2836. https://doi.org/10.1016/j.aej.2016.08.025

Jha, B. K., & Oni, M. O. (2019). Natural convection flow in a vertical annulus with time-periodic thermal boundary conditions: An exact solution. Propulsion and Power

Research, 8(1), 47–55. https://doi.org/10.1016/j.jppr.2018.12.002

Jha, B. K., Oni, M. O., Abba, J. M., & Mundi, B. I. (2024). Unsteady natural convection flow in a vertical tube inspired by ramped surface temperature of the tube. International Journal of Magnetics and Electromagnetism, 10, 043. https://doi.org/10.35840/2631-5068/6543

Kataria, H. R., & Patel, H. (2019). Effects of chemical reaction and heat generation/absorption on MHD Casson fluid flow past an exponentially accelerated vertical plate embedded in porous medium with ramped wall temperature and ramped surface concentration. Propulsion and Power Research, 8(1), 35–46. https://doi.org/10.1016/j.jppr.2018.11.001

Khadrawi A. F, Al-Nimr M. A, (2007) Unsteady Natural Convection Fluid Flow in a Vertical Microchannel under the Effect of the Dual-Phase-Lag Heat-Conduction Model. *Int. J. Thermo Physics*; 28(4): 1387-1400.

Kumar, A. (2016). Effect of radial magnetic field on free convective flow over ramped-velocity moving vertical cylinder with ramped-type temperature and concentration. Journal of Applied Fluid Mechanics, 9(6), 2855–2864. https://doi.org/10.29252/jafm.09.06.26060

Molla, M. M., Hossain, M. A., & Yao, L. S. (2004). Natural convection flow along a vertical wavy surface with uniform surface temperature in presence of heat generation/absorption. International Journal of Thermal Sciences, 43(2), 157–163.

Pal, D., & Mondal, H. (2011). Effects of Soret, Dufour, chemical reaction and thermal radiation on unsteady MHD non-Darcy mixed convection. Communications in Nonlinear Science and Numerical Simulation, 16(4), 1942–1957. https://doi.org/10.1016/j.cnsns.2010.08.023

Parasuraman, L., & Babu, V. (2024). Point/line heat-source configuration with buoyancy and mass transfer in a vertical channel. International Communications in Heat and Mass Transfer, 158, 107943. https://doi.org/10.1016/j.icheatmasstransfer.2024.107943

Shah, S. S., Öztop, H. F., Ul-Haq, R., & Abu-Hamdeh, N. (2023). Natural convection process endorsed in coaxial duct with Soret/Dufour effect. International Journal of Numerical Methods for Heat & Fluid Flow, 33(1), 96–115. https://doi.org/10.1108/HFF-02-2022-0106

Tayebi, T., El-Sapa, S., Karimi, N., Dogonchi, A. S., Sheremet, M. A., & Pop, I. (2023). Double-diffusive natural convection with Soret/Dufour effects and energy optimization of nano-encapsulated phase change material in a novel form of a wavy-walled I-shaped domain. Journal of the Taiwan Institute of Chemical Engineers, 148, 104873. https://doi.org/10.1016/j.jtice.2023.104873

Tzou D. Y., (1997) Macro- to Microscale Heat Transfer: The Lagging Behavior (Taylor and Francis, Washington, DC, pp. 1–64

Umavathi, J. C., & Bég, O. A. (2022). Computation of thermo-solutal convection with Soret–Dufour cross-diffusion in a vertical duct containing carbon/metallic nanofluids. Proceedings of the Institution of Mechanical Engineers, Part C: Journal of Mechanical Engineering Science, 236(13), 7456–7472.

Vanita, & Kumar, A. (2016). Effect of radial magnetic field on natural convection flow in alternate conducting vertical concentric annuli with ramped temperature. Engineering Science and Technology, an International Journal, 19(3), 1436–1451. https://doi.org/10.1016/j.jestch.2016.04.010

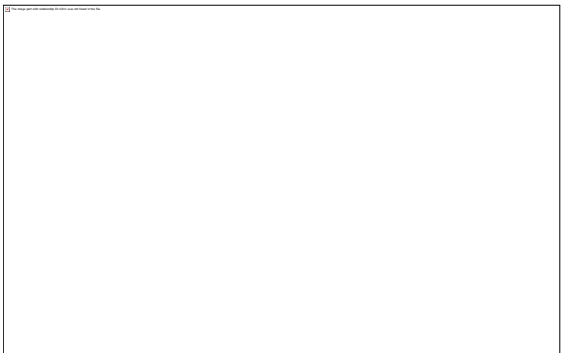

Figure 1: Display of the physical problem

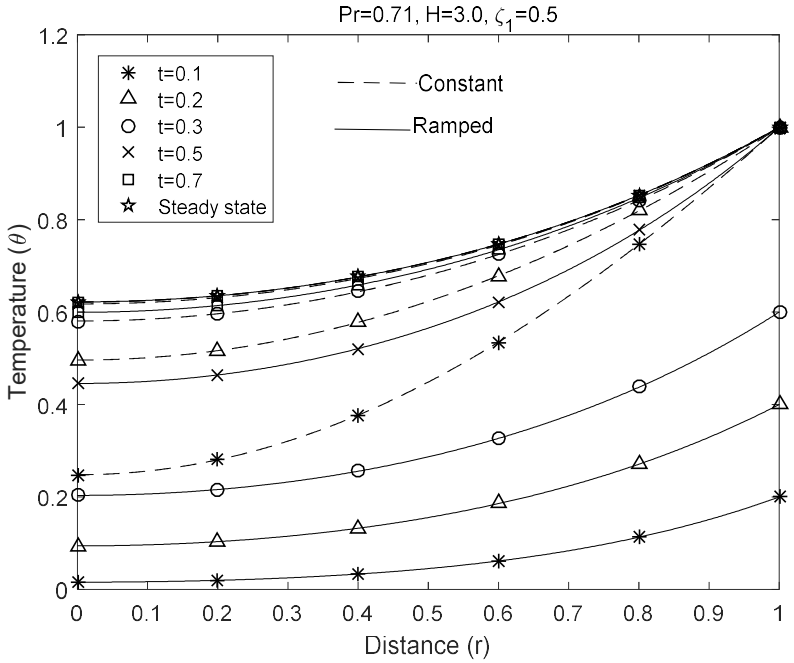

Figure 21: Temperature profiles for a variable time ( )

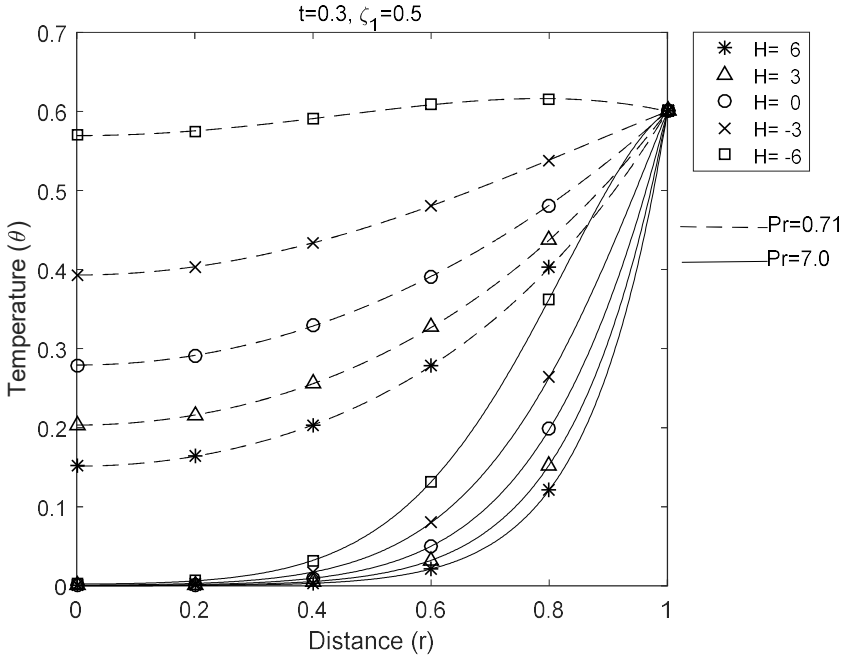

Figure 3: Temperature profiles for different values Prand

https://doi.org/10.5281/zenodo.17251831

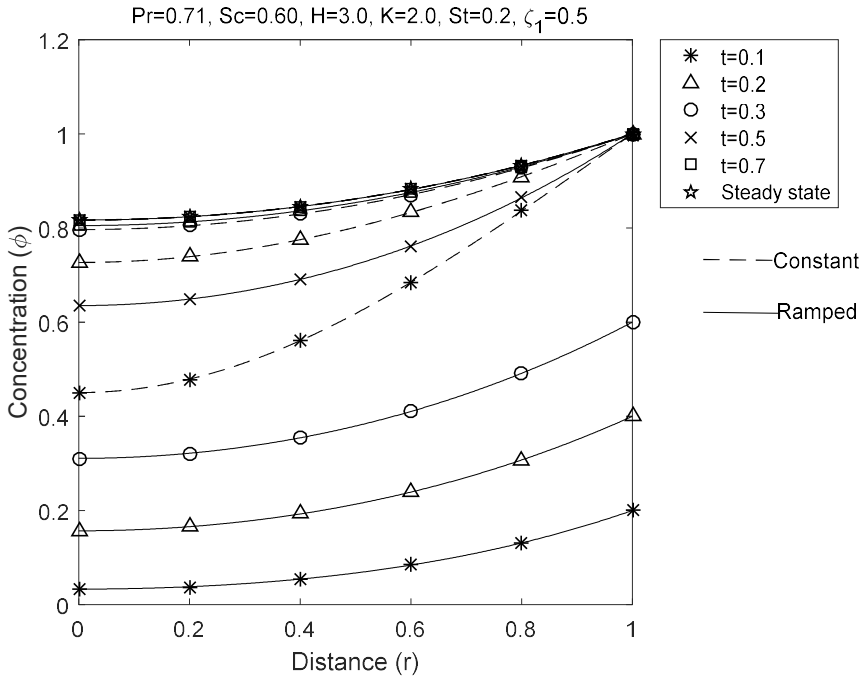

Figure 4: Concentration profiles for a variable time(□)

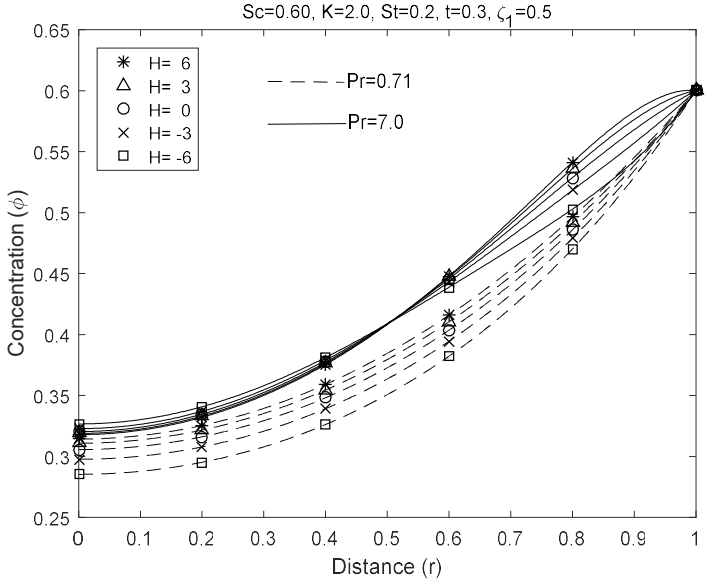

Figure 5: The effect of □ and □□ on the concentration profiles

https://doi.org/10.5281/zenodo.17251831

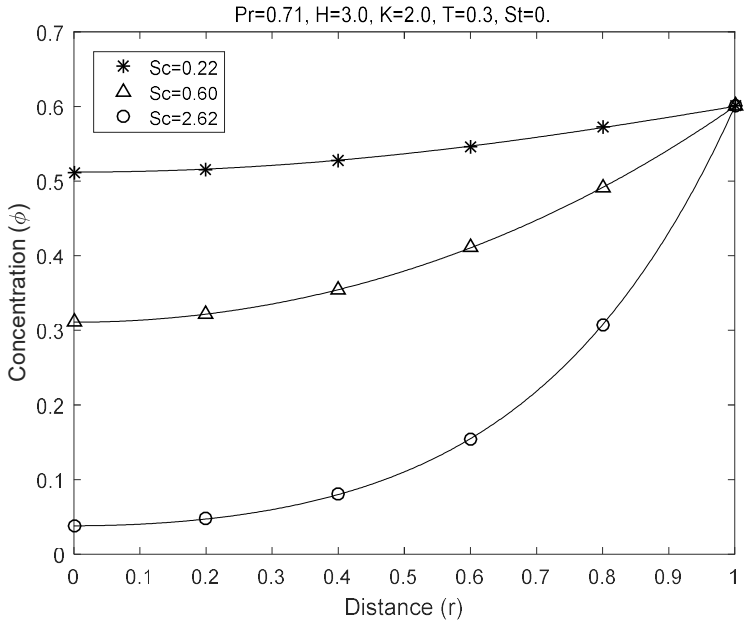

Figure 6: Concentration profiles for various values of Schmidt number (□□)

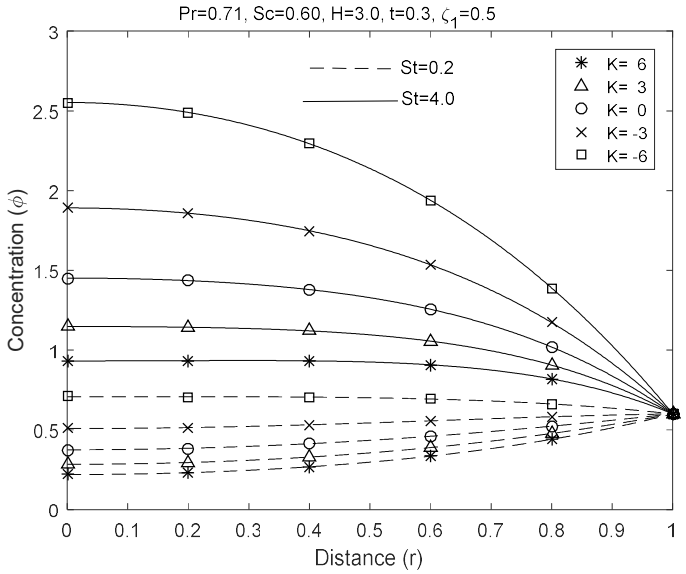

Figure 7: The impact of chemical reaction (□) and Soret number (□□) on the concentration

https://doi.org/10.5281/zenodo.17251831

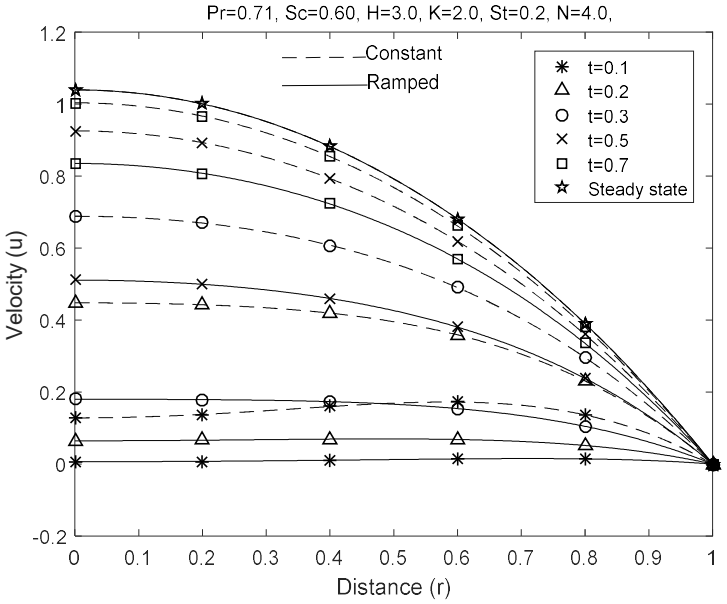

Figure 8: The effect of varying □ on the velocity

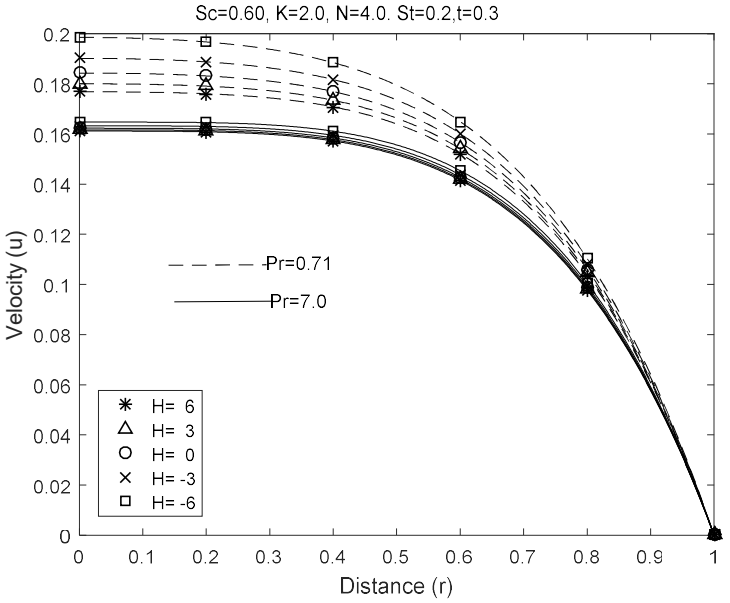

Figure 9: The effect of □□ and □ on the velocity

https://doi.org/10.5281/zenodo.17251831

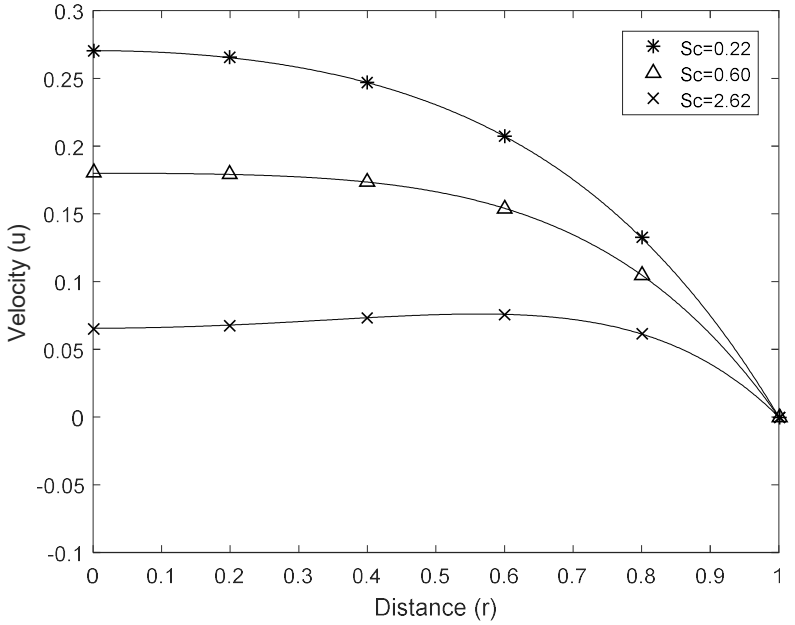

Figure 10: The effect of □□ on the velocity

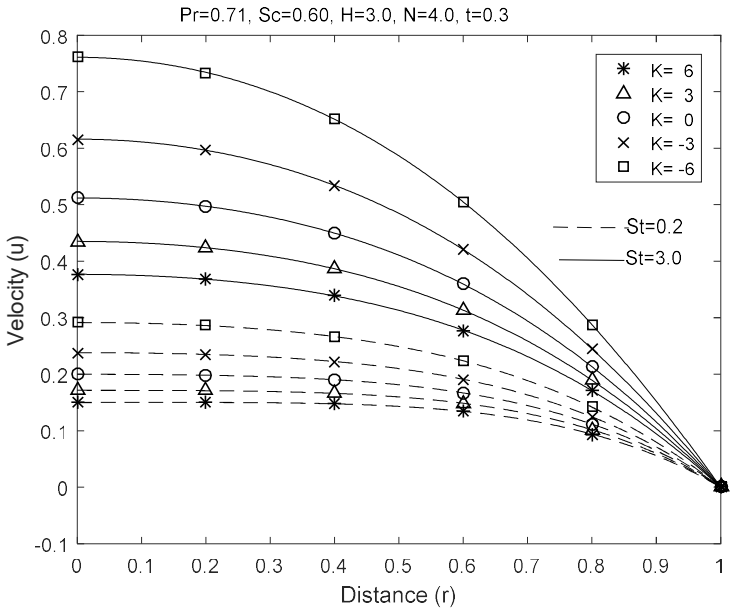

Figure 11: Velocity profiles for different values of chemical reaction(□)

Parameter		*Nu*	*Sh*	*τ*	**Parameter**		*Sh*	*τ*
	0.2	0.7801	0.5302	0.3909		6	0.9615	0.6649
	0.3	0.9701	0.6167	0.7186		3	0.7098	0.7037
t	0.5	1.3175	0.7666	1.4997	*K*	0	0.4132	0.7522
	0.7	0.8834	0.3884	1.9619		-3	0.0512	0.8146
	1	0.8562	0.3736	2.1707		-6	-0.4100	0.8972
Pr	0.71	0.9701	0.6167	0.7186	*Sc*	0.22	0.1468	0.8491
	7	3.8622	0.1001	0.6857		0.6	0.6167	0.7186

https://doi.org/10.5281/zenodo.17251831

	6	1.2287	0.5762	0.7137		0.2	0.6167	0.7186
	3	0.9701	0.6167	0.7186	*St*	0.5	0.3890	0.7663
H	0	0.6674	0.6621	0.7250		0.8	0.1612	0.8139
	-3	0.3000	0.7140	0.7335				
	-6	-0.1655	0.7750	0.7453				

Table 1: Effect of the flow parameters on the skin-friction, Nusselt, and Sherwood numbers on the wall of the tube when □□ = 0.71, □□ = 0.60, □ = 0.2, □ = 3.0, □ = 2.0, □$_1$ = *0.5*

		Velocity				**Velocity**		
t	***r***	*RSA*	*PDEPE*	***t***	***r***	*RSA*	*PDEPE*	*ES*
0.2	0	0.0646	0.0646	0.8	0	0.9224	0.9226	
	0.2	0.0662	0.0661		0.2	0.8901	0.8902	
	0.4	0.0693	0.0688		0.4	0.7907	0.7907	
	0.6	0.0682	0.0674		0.6	0.6173	0.6171	
	0.8	0.0516	0.0508		0.8	0.3586	0.3585	
0.4	0	0.334	0.3341	2	0	1.0396	1.0212	
	0.2	0.3283	0.3285		0.2	1.0006	0.9832	
	0.4	0.3077	0.3078		0.4	0.8823	0.8678	
	0.6	0.2609	0.2611		0.6	0.6810	0.6708	
	0.8	0.1683	0.1686		0.8	0.3900	0.3850	
0.6	0	0.6951	0.6954	2.4	0	1.0396	1.0214	1.0396
	0.2	0.6755	0.6756		0.2	1.0006	0.9834	1.0006
	0.4	0.6124	0.6122		0.4	0.8823	0.8679	0.8823
	0.6	0.4929	0.4925		0.6	0.6810	0.6709	0.6810
	0.8	0.2971	0.2968		0.8	0.3900	0.3851	0.3900

Table 2: Numerical comparison of Riemann sum approximation method (□□□) solutions, □□□□□ and steady-state exact solutions (□□)(□□ = *0.71*, □□ = *0.60*, □ = *3*, □ = *2*, □□ = *0.2*, □ = *4*)

https://doi.org/10.5281/zenodo.17251831